

Combined Al and C alloying enables mechanism-oriented design of multi-principal element alloys

Ab initio calculations and experiments

Kies, Fabian; Ikeda, Yuji; Ewald, Simon; Schleifenbaum, Johannes H.; Hallstedt, Bengt; Körmann, Fritz; Haase, Christian

DOI

[10.1016/j.scriptamat.2019.12.004](https://doi.org/10.1016/j.scriptamat.2019.12.004)

Publication date

2020

Document Version

Final published version

Published in

Scripta Materialia

Citation (APA)

Kies, F., Ikeda, Y., Ewald, S., Schleifenbaum, J. H., Hallstedt, B., Körmann, F., & Haase, C. (2020). Combined Al and C alloying enables mechanism-oriented design of multi-principal element alloys: Ab initio calculations and experiments. *Scripta Materialia*, 178, 366-371. <https://doi.org/10.1016/j.scriptamat.2019.12.004>

Important note

To cite this publication, please use the final published version (if applicable). Please check the document version above.

Copyright

Other than for strictly personal use, it is not permitted to download, forward or distribute the text or part of it, without the consent of the author(s) and/or copyright holder(s), unless the work is under an open content license such as Creative Commons.

Takedown policy

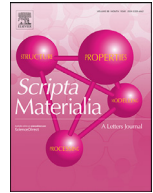
Please contact us and provide details if you believe this document breaches copyrights. We will remove access to the work immediately and investigate your claim.

Green Open Access added to TU Delft Institutional Repository

'You share, we take care!' - Taverne project

<https://www.openaccess.nl/en/you-share-we-take-care>

Otherwise as indicated in the copyright section: the publisher is the copyright holder of this work and the author uses the Dutch legislation to make this work public.



Combined Al and C alloying enables mechanism-oriented design of multi-principal element alloys: *Ab initio* calculations and experiments

Fabian Kies^{a,*}, Yuji Ikeda^{b,c}, Simon Ewald^d, Johannes H. Schleifenbaum^{d,e}, Bengt Hallstedt^f, Fritz Körmann^{b,g}, Christian Haase^{a,*}

^aSteel Institute (IEHK), RWTH Aachen University, 52072 Aachen, Germany

^bComputational Materials Design, Max-Planck-Institut für Eisenforschung GmbH, 40237 Düsseldorf, Germany

^cInstitute for Materials Science (IMW), University of Stuttgart, 70569 Stuttgart, Germany

^dDigital Additive Production (DAP), RWTH Aachen University, 52074 Aachen, Germany

^eFraunhofer Institute for Laser Technology (ILT), 52074 Aachen, Germany

^fMaterials Applications in Mechanical Engineering (IWM), RWTH Aachen University, 52062 Aachen, Germany

^gMaterials Science and Engineering, Delft University of Technology, 2628 CD Delft, The Netherlands

ARTICLE INFO

Article history:

Received 8 August 2019

Revised 1 December 2019

Accepted 2 December 2019

Available online 12 December 2019

Keywords:

Multi-principal element alloy

High-entropy alloy

Additive manufacturing

Density functional theory (DFT)

Mechanical properties

ABSTRACT

Density functional theory (DFT) calculations were performed on $Al_xC_yCoFeMnNi$ multi-principal element alloys (MPEAs) to understand the influence of Al and C on the stacking-fault energy (SFE). C addition to CoFeMnNi resulted in increased SFE, while it decreased in Al-alloyed CoFeMnNi. For experimental verification, $Al_{0.26}C_yCoFeMnNi$ with 0, 1.37 and 2.70 at% C were designed by computational thermodynamics, produced by additive manufacturing (AM) and characterized by tensile tests and microstructure analysis. Twinning-induced plasticity (TWIP) was enhanced with increased C, which confirmed a decreased SFE. The combination of these methods provides a promising toolset for mechanism-oriented design of MPEAs with advanced mechanical properties.

© 2019 Acta Materialia Inc. Published by Elsevier Ltd. All rights reserved.

Multi-principal element alloys (MPEAs), also known as high-entropy alloys (HEAs), are a comparatively new class of alloys, which recently gained much attention in both academia and industry. This interest is mainly originating from the new possibilities that are related to the almost infinite number of chemical compositions and thus materials properties [1–4]. Instead of relying on one base element, MPEAs are defined by consisting of multiple elements, each with fractions between 5 and 35 at% [5]. The philosophy behind MPEAs lies in its large degree of freedom in their design, as multiple substitutional and interstitial elements can be varied depending on the requirements of the target application. Especially interesting for structural applications is the adjustment of their stacking-fault energy (SFE), which determines the activation or suppression of plastic deformation mechanisms such as dislocation slip, transformation- (TRIP) or twinning-induced plasticity (TWIP) [6–8]. In high-Mn steels, this method was already effectively used to tailor the mechanical properties [9] and similar attempts have been made towards mechanisms-based design

of MPEAs [10,11]. However, the number of possible elemental combinations of MPEAs makes tailoring of individual properties challenging, as it requires powerful screening methods to efficiently explore the alloying space [12,13]. Previously, we suggested a methodology combining thermodynamic modeling with additive manufacturing (AM) using elemental powder blends [14–16] to rapidly screen MPEAs. A new CALPHAD database was compiled from all binary and available ternary systems of CoCrFeMnNi, which largely do not contain hexagonally closest packed (hcp) phases. However, the consideration of hcp is essential for the calculation of SFEs [17] and the prediction of the occurring deformation mechanisms. In contrast, *ab initio* calculations based on the density functional theory (DFT) have emerged as a powerful tool to investigate MPEAs [18] and have been previously used to compute SFEs [18–36]. A successful combination of the aforementioned methods, i.e. DFT-based SFE calculations with CALPHAD- and AM-based alloy screening, may open up a new way for precise and efficient exploration of novel MPEAs with advanced mechanical properties.

In this study, the influence of Al and C on the SFE in the CoFeMnNi alloy was investigated theoretically and experimentally. The alloy was chosen based on CALPHAD calculations, where the elimination of Cr from the widely used CoCrFeMnNi system

* Corresponding authors.

E-mail addresses: fabian.kies@iehk.rwth-aachen.de (F. Kies), christian.haase@iehk.rwth-aachen.de (C. Haase).

prevents carbide formation and increases the solubility of C in the face-centered cubic (fcc) phase. A recent *ab initio* study demonstrated that C increases the SFE of CoCrFeMnNi [34]. To the best of the authors' knowledge however, such *ab initio* SFE calculations have not yet been reported for MPEAs containing Al and C. Specifically the addition of Al is of high interest, as it decreases density, influences phase stability and SFE, and improves the resistance against hydrogen embrittlement in high-Mn steels [5,37,38]. Consequently, DFT-based SFE modeling was performed with C additions to CoFeMnNi and Al-alloyed CoFeMnNi. The results were applied to the CALPHAD and AM approach for experimental characterization and validation, where $\text{Al}_{0.26}\text{C}_y\text{CoFeMnNi}$ samples with 0, 1.37 and 2.70 at% C were produced by laser powder bed fusion (LPBF). Tensile testing and electron backscatter diffraction (EBSD) analyses were performed and correlated with the DFT results to better understand the relationship between chemical composition and activated deformation mechanisms.

The SFEs of the fcc alloys were evaluated from the DFT energies of the fcc and hcp phases. These calculations were based on the first-order axial Ising model (AIM1) [39]. Both CoFeMnNi and $\text{Al}_{0.5}\text{CoFeMnNi}$ were modeled using 54-atom supercells to evaluate the impact of Al. The high Al concentration in $\text{Al}_{0.5}\text{CoFeMnNi}$ was chosen to ensure an effective sampling of interstitial sites with Al-containing nearest-neighbor shells. The employed supercells for the fcc and the hcp phases had identical cell shapes to improve the computational efficiency. Ideal mixing of the elements was approximated based on special quasi-random structures (SQSs) [40]. The solution energies ΔE_{sol} of C atoms were computed as

$$\Delta E_{\text{sol}} = E(\text{alloy} + \text{C}) - [E(\text{alloy}) + E(\text{C})], \quad (1)$$

where $E(\text{alloy} + \text{C})$ and $E(\text{alloy})$ are the energies of the alloys per simulation cell with and without one C atom, respectively. $E(\text{C})$ denotes the energy of C per atom in the reference state graphite. Octahedral sites surrounded by six atoms in the first nearest-neighbor shell were considered as interstitial sites for C. To investigate the local-environment dependence of C solution energies in the MPEAs, 324 different octahedral sites were computed for each alloy and for each phase. The projector augmented-wave (PAW) method [41] was employed within the generalized gradient approximation (GGA) of the Perdew-Burke-Ernzerhof (PBE) form [42], as implemented in the VASP code [43–45]. Spin-polarization was considered, as this is known to affect the phase stability of 3d-transition-element MPEAs [18,46]. Ionic relaxations were performed until the residual forces became less than $5 \times 10^{-2} \text{ eV}\text{\AA}^{-1}$, while the volumes and shapes of the supercell models were kept fixed to the fcc lattice constant of 3.6 Å throughout the calculations. Further computational details can be found in the supplementary material.

For the experimental investigation, single-phase fcc alloys were identified within the $\text{Al}_x\text{C}_y\text{CoFeMnNi}$ system by CALPHAD calculations using Thermo-Calc (Fig. 1). The maximum solubility of Al in the fcc matrix was predicted to be around 3 wt%, whereas a B2 phase may be expected at higher Al contents. Cylindrical samples were manufactured on an AconityMINI LPBF machine by Aconity3D using elemental powder blends. This method can be reliably used to generate fully dense samples without macro-segregation and only minor, regularly distributed micro-segregation, as previously shown in [16]. These were generated with 200 W laser power, 550 mm s⁻¹ scanning speed, 60 μm hatch distance and 30 μm layer thickness for equiatomic CoFeMnNi samples with 3 wt% Al and 0, 0.3 and 0.6 wt% C (Table 1). The alloys are denoted as $\text{Al}^6\text{-C}^{0.0}$, $\text{Al}^6\text{-C}^{1.4}$ and $\text{Al}^6\text{-C}^{2.7}$ according to the atomic percentages added to CoFeMnNi. The generated cylinders were machined to B4×20 tensile specimens and quasi-static uniaxial tensile testing was performed on a Z4204 Zwick/Roell at room temperature with a strain rate of $2.5 \times 10^{-4} \text{ s}^{-1}$. Samples were prepared by

Table 1
Chemical composition of the investigated samples.

Sample	Al	C	Co	Fe	Mn	Ni
$\text{Al}^6\text{-C}^{0.0}$ (at%)	6.14	0.00	23.5	23.5	23.5	23.5
$\text{Al}^6\text{-C}^{1.4}$ (at%)	6.08	1.37	23.1	23.1	23.1	23.1
$\text{Al}^6\text{-C}^{2.7}$ (at%)	6.01	2.70	22.8	22.8	22.8	22.8
$\text{Al}^6\text{-C}^{0.0}$ (wt%)	3.00	0.00	25.0	23.7	23.3	24.9
$\text{Al}^6\text{-C}^{1.4}$ (wt%)	3.00	0.30	25.0	23.6	23.3	24.8
$\text{Al}^6\text{-C}^{2.7}$ (wt%)	3.00	0.60	24.9	23.6	23.2	24.8

mechanical grinding with up to 1200 SiC grit paper and polishing with 6 and 1 μm diamond suspension. Electrolytical polishing was performed at 30–25 V for 15 s using Struers A2 electrolyte. EBSD data was recorded on a Zeiss-Sigma field emission gun (FEG) scanning electron microscope (SEM) using a detector by Oxford Instruments. A voltage of 15 kV, working distance of 17–18 μm and step size of 60 nm were chosen. Analysis and noise reduction were carried out with the MATLAB® based MTEX toolbox [47,48].

The distribution of solution energies for interstitial C atoms at the octahedral sites obtained by the DFT calculations are shown in Fig. 2a and Fig. 2b for CoFeMnNi and $\text{Al}_{0.5}\text{CoFeMnNi}$, respectively. For CoFeMnNi, large standard deviations (SDs) of 0.367 and 0.326 eV for the solution energies in the fcc and hcp phase were found. This indicates a strong dependence of the solution energies on the specific local environment around the C atoms. The average solution energies were in total 0.322 eV lower in the fcc phase compared to the hcp phase. This implies that C atoms energetically stabilize the fcc phase over the hcp phase, similarly as previously found for CoCrFeMnNi [34]. For $\text{Al}_{0.5}\text{CoFeMnNi}$, the SDs of the solution energies (0.418 and 0.520 eV for the fcc and hcp phases, respectively) were substantially larger than those for CoFeMnNi, indicating an even stronger dependence of the solution energies on the local environment of C atoms. The average solution energies were found to be 0.060 eV higher in the fcc phase than in the hcp phase. This indicates that C atoms energetically stabilize the hcp phase over the fcc phase, which is the opposite trend as in the Al-free CoFeMnNi alloy. It was also observed that the C solution energies tend to be lower with fewer Al atoms within the first nearest-neighbor shell around the C atoms. This again implies a strong dependence of C solution energies on its local chemical environment.

Table 2 summarizes the *ab initio* SFEs of the investigated alloys and pure Al for comparison. CoFeMnNi without C had a SFE of 32 mJ m⁻², which is more than 30 mJ m⁻² higher than the SFE of CoCrFeMnNi without C at the same lattice constant [34]. This implies that the addition of Cr decreases the SFE. Similar trends on the impact of Cr have been also found in other 3d-transition-element alloys (e.g. comparisons of CoNi and CoCrNi, CoFeNi and CoCrFeNi, CoFeMnNi and CoCrFeMnNi in Fig. 2 by Zhao et al. [26]). For $\text{Al}_{0.5}\text{CoFeMnNi}$ without C, the SFE was 51 mJ m⁻². This is substantially higher than the one obtained for the Al-free CoFeMnNi alloy, indicating that Al is likely to increase the SFE of CoFeMnNi. Note that the SFEs were computed at 0 K; finite-temperature excitations like lattice vibrations [18,26,33,49,50] and magnetic fluctuations [18,20,29,50] could modify the absolute values of SFEs. It is interesting to note that, in the spirit of Vegard's law, the SFE of the $\text{Al}_{0.5}\text{CoFeMnNi}$ alloy can be constructed from the weighted average of the SFEs of Al and CoFeMnNi. Due to C additions of 1.00, 1.37 and 2.70 at%, the SFE of CoFeMnNi increased by 19, 25 and 51 mJ m⁻², respectively. These values are indeed more than twice larger as the ones found for CoCrFeMnNi [34]. In contrast, C additions of 1.00, 1.37 and 2.70 at% to $\text{Al}_{0.5}\text{CoFeMnNi}$ decreased the SFE by 4, 5 and 10 mJ m⁻², respectively. This indicates that the interaction between Al and C reduces the SFE of $\text{Al}_{0.5}\text{CoFeMnNi}$. As

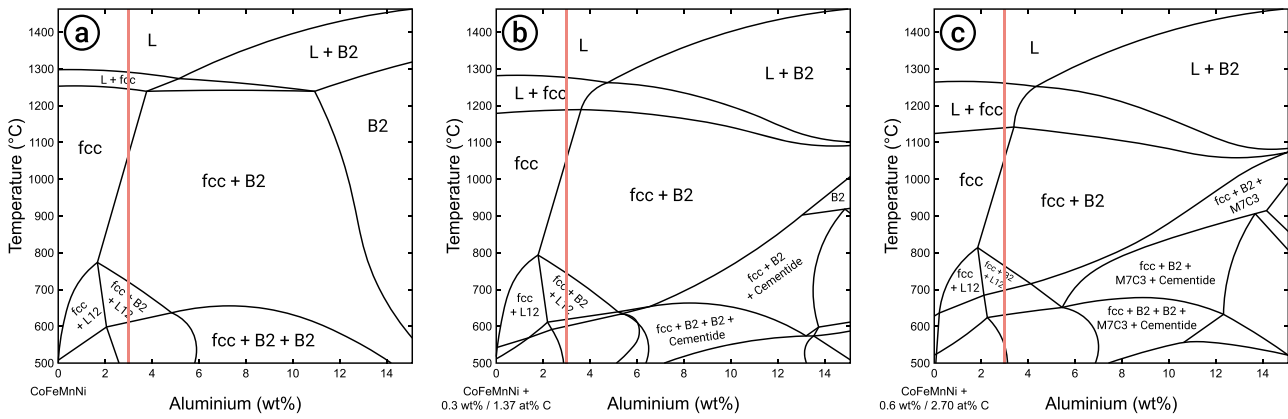


Fig. 1. Phase diagrams as a function of the Al content for (a) CoFeMnNi, (b) CoFeMnNi + 0.3 wt% C and (c) CoFeMnNi + 0.6 wt% C. The chosen MPEAs are highlighted at 3 wt% Al, where the alloys are expected to be single-phase fcc after rapid cooling in LPBF.

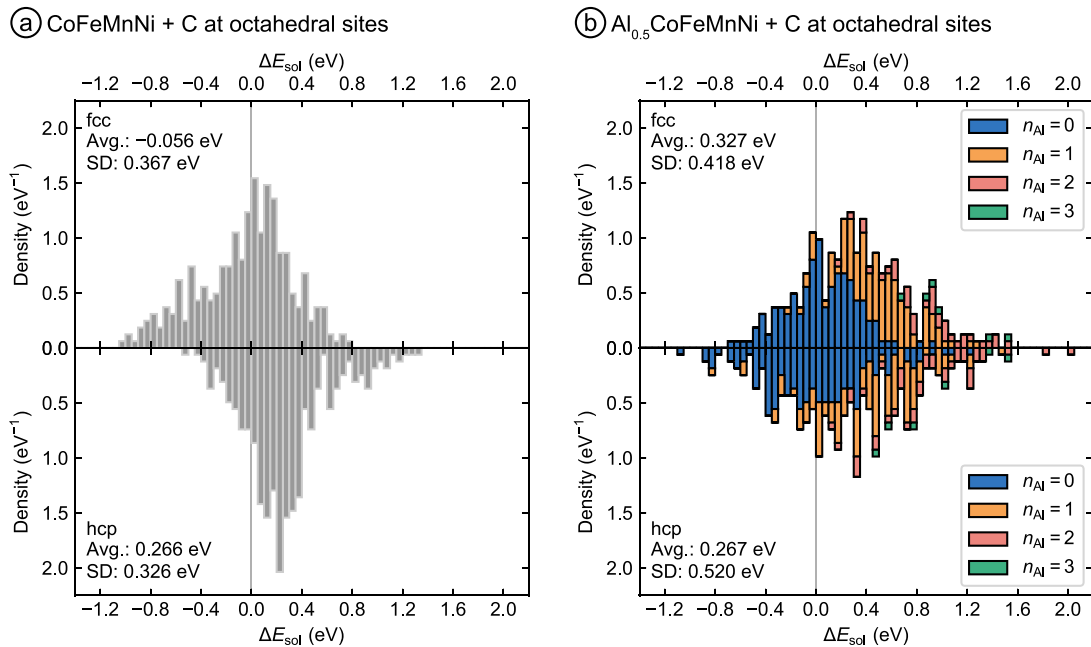


Fig. 2. Distribution of C solution energies at the octahedral sites in (a) CoFeMnNi and (b) $\text{Al}_{0.5}\text{CoFeMnNi}$ obtained from *ab initio* calculations. The upper and the lower panels show the results for the fcc and the hcp phase, respectively. The average (avg.) and the standard deviation (SD) of the solution energies are also shown in the panels. For $\text{Al}_{0.5}\text{CoFeMnNi}$, the colors of the histogram distinguish the number of Al in the first nearest-neighbor shell (n_{Al}) of the C atom.

Table 2

Computed SFEs (mJ m^{-2}) of the investigated alloys and Al at different C contents, including the experimentally used amounts of 1.37 and 2.70 at%. The volumes correspond to the fcc lattice constant of 3.6 Å, which was used for the calculations. The unexpected decrease of the SFE in $\text{Al}_{0.5}\text{CoFeMnNi}$ can be qualitatively understood by the impact of C on the SFE of pure Al.

Carbon	–	1.00 at%	1.37 at%	2.70 at%
CoFeMnNi	32	51	57	83
$\text{Al}_{0.5}\text{CoFeMnNi}$	51	47	46	41
Al [†]	221	187	174	127

[†] Note that at the equilibrium lattice constant of Al, the SFE is about 149 mJ m^{-2} [51].

described in the following, the experimental investigations confirm the observed trends.

The results of the tensile tests are shown in Fig. 3. An increase in the C content from 0–2.70 at% increased the yield strength $R_{p0.2}$ from 397 to 472 MPa, ultimate tensile strength R_m from 620 to 820 MPa and uniform elongation from 26.2 to 39.2 % (Fig. 3a). Furthermore, the slope of the strain hardening rate (Fig. 3b) de-

creased. Whereas the curve in $\text{Al}^6\text{-C}^{0.0}$ decreased steadily in its strain hardening rate, a plateau-like region was observed in $\text{Al}^6\text{-C}^{1.4}$ and $\text{Al}^6\text{-C}^{2.7}$ in the strain range between 0.05 and 0.15. Additionally, $\text{Al}^6\text{-C}^{2.7}$ revealed an overall higher strain hardening rate than $\text{Al}^6\text{-C}^{1.4}$.

The microstructures after deformation close to the fracture surfaces of the tensile specimens are shown in Fig. 4. All investigated samples contained a single-phase fcc microstructure. Small amounts of deformation-induced twins were detected in $\text{Al}^6\text{-C}^{0.0}$ and $\text{Al}^6\text{-C}^{1.4}$. The fraction of deformation twins strongly increased in $\text{Al}^6\text{-C}^{2.7}$. The EBSD-microtexture of the matrix without the consideration of deformation twins (Fig. 4g–i) showed {111}-fibers, which was weakest in $\text{Al}^6\text{-C}^{2.7}$.

The yield strength increased in the $\text{Al}_{0.26}\text{C}_y\text{CoFeMnNi}$ alloys by solid solution hardening with around 32 MPa at%⁻¹ or 148 MPa wt%⁻¹ C in solution, which is lower than in austenitic steels (~77 MPa at%⁻¹) [9] or other alloys in the CoCrFeMnNi system (~65 MPa at%⁻¹) [52–59]. However, solid solution hardening in CoCrFeMnNi with C was only observed to a small extent, as contents of 1 at% already led to carbide precipitation. Therefore, C

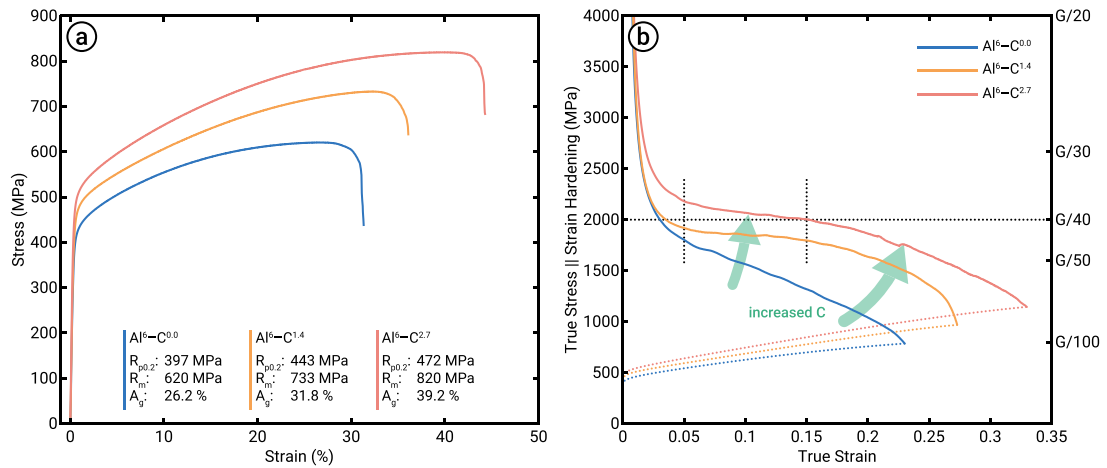


Fig. 3. (a) Engineering stress-strain, (b) true stress (dotted) and strain hardening rate-true strain (solid) curves for the tensile tested samples. Yield strength $R_{p0.2}$, ultimate tensile strength R_m and uniform elongation A_g were increased with higher carbon content in the alloys. In the strain hardening curve, a weaker decline was observed in Al⁶-C^{1.4} and Al⁶-C^{2.7} at around 1/40 of the shear modulus G .

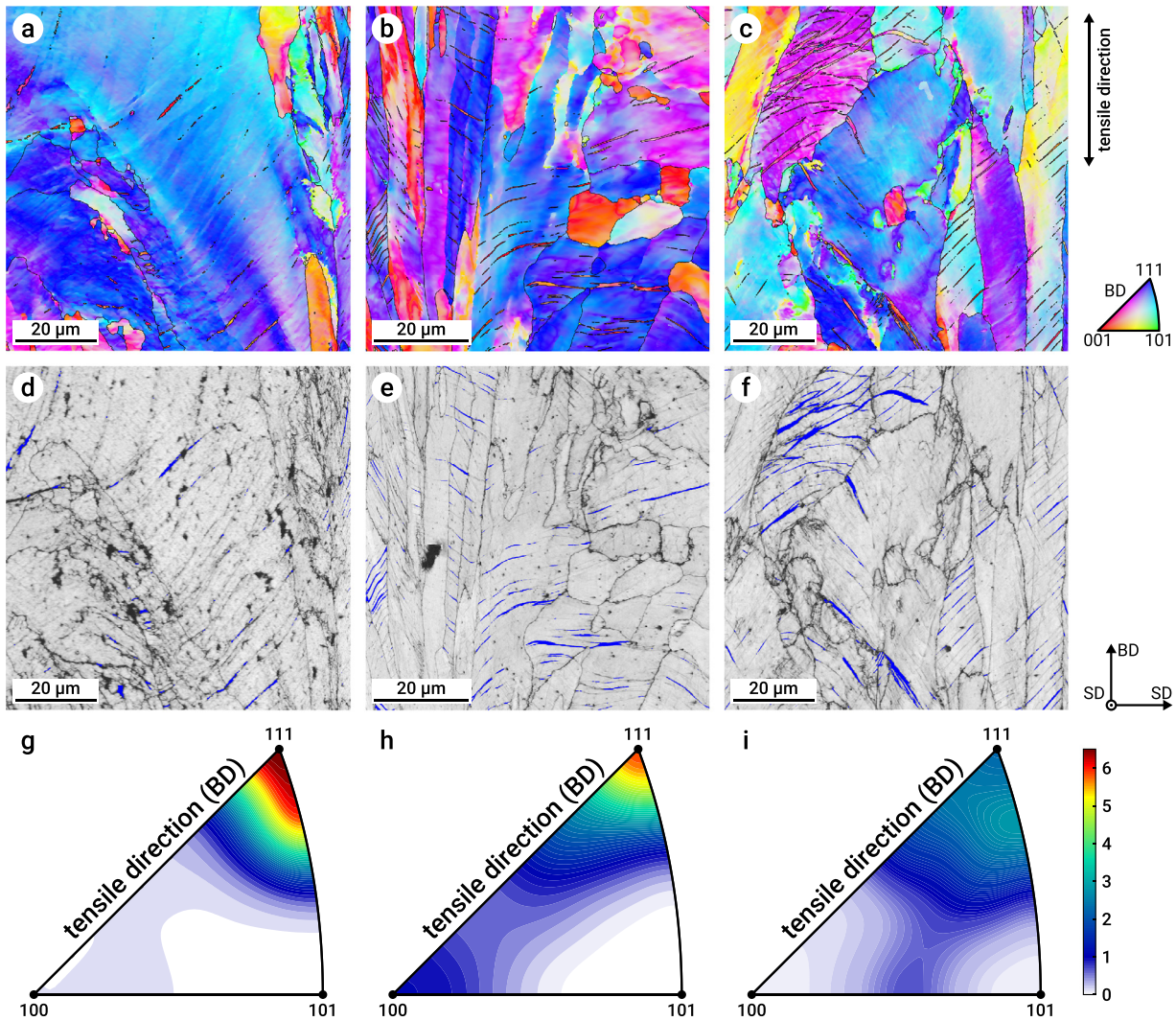


Fig. 4. EBSD analyses of (a, d, g) Al⁶-C^{0.0}, (b, e, h) Al⁶-C^{1.4} and (c, f, i) Al⁶-C^{2.7} close to the fracture surfaces of the tensile samples. BD and SD denote the build-up and scanning direction, respectively. (a–c) Inverse pole figure overlay of fcc in BD, where black lines denote general high-angle ($>10^\circ$) grain boundaries. (d–f) Band contrast maps overlaid with deformation twins (detection with $\Sigma 3$ grain boundaries (60° around 111) with 5° tolerance) in blue. (g–i) Corresponding microtexture analysis for the areas excluding deformation twins. (For interpretation of the references to color in this figure legend, the reader is referred to the web version of this article.)

can be effectively used in the $\text{Al}_x\text{C}_y\text{CoFeMnNi}$ system to increase strength, as the absence of Cr prevents formation of carbides.

Surprisingly, the addition of C also resulted in higher ductility, which is the opposite effect expected from the impeded dislocation glide by solid solution hardening. The activation of TWIP may explain this behavior, which was observed in the deformed microstructure and is known to promote increased ductility and ultimate tensile strength [9]. Consequently, several strain hardening stages are typically obtained [8,60–62]. Plateau formation after the first steep decline coincides with the evolution of a dislocation substructure at around $G/40$, after which the strain hardening rate increases again due to dislocation interaction with twin-bundles. Once the dislocation and twin-bundle density saturate in stored dislocations, i.e. the maximum capability for trapping further dislocations, is achieved, the strain hardening rate decreases again. In relation to the investigated alloys, $\text{Al}^6\text{-C}^{0.0}$ shows the typical progression for medium to high SFE fcc alloys predominantly deforming by dislocation glide, where the strain hardening rate decreases steadily during deformation [63]. Consequently, the deformed microstructure showed negligible amounts of deformation-induced twins. In $\text{Al}^6\text{-C}^{1.4}$ and $\text{Al}^6\text{-C}^{2.7}$ however, a plateau-like region was observed in the strain hardening curve after the initial steep decline. Compared to the shear modulus, which was assumed to be similar to the CoCrFeMnNi alloy with 80 GPa [64,65], the plateau-like region indeed occurred at around $G/40$. Furthermore, the level of this region increased with C content, which can be attributed to decreased SFE, temperature, grain size or strain rate [8]. Since the same testing conditions and LPBF processing parameters were used, i.e. temperature, grain size and strain rate remained constant, a decrease in SFE must have been responsible for this behavior. Due to the same processing parameters, the amount and amplitude of micro-segregation [16] is equal in the samples with varying chemical composition. These micro-segregations are very small in LPBF-produced metals in contrast to laser metal deposition [15,66]. As a consequence, the development and appearance of deformation-induced twins was not impeded [67]. Furthermore, the fraction of deformation twins increased with increasing C content (Fig. 4d–f). It is well known that deformation twinning strongly depends on the respective crystal orientation. In the present study, $\text{Al}^6\text{-C}^{2.7}$ showed a weaker $\{111\}\parallel\text{BD}$ -fiber compared to $\text{Al}^6\text{-C}^{0.0}$ and $\text{Al}^6\text{-C}^{1.4}$ (Fig. 4g–i). According to Gutierrez-Urrutia et al. [68], $\{111\}$ -oriented grains are favorable for deformation twinning due to the high Schmid factor for twinning. Therefore, the higher twin volume fraction combined with a less favorable texture for deformation twinning in $\text{Al}^6\text{-C}^{2.7}$ proves that the enhanced TWIP effect in this MPEA is not a texture effect, but indeed a result of the decreased SFE with increased C content.

As shown in Fig. 3, the addition of C to the investigated $\text{Al}_{0.26}\text{C}_y\text{CoFeMnNi}$ alloy enables an increase in both strength and ductility, i.e. overcoming the strength-ductility trade-off. This behavior can undoubtedly be correlated with the increased contribution of TWIP to the accommodation of plastic deformation (see Fig. 4), which results from a decrease in SFE, as predicted by the DFT calculations. Additionally, solid solution strengthening and the formation of C-Mn clusters further promote TWIP due to a higher critical resolved shear stress [9] and an increased stacking fault width resulting from dislocation pinning [69]. Although the positive effect of deformation-induced twinning on the mechanical properties of fcc metals is well known, the reversed influence of C on the SFE is quite surprising. Usually, an increase in SFE with increasing C content was reported, for instance in high-Mn steels [7], the Cantor MPEA [34] and in the Al-free CoFeMnNi MPEA in this study (see Table 2). Consequently, the addition of C to MPEAs increases the strength due to solid solution strengthening, but also causes reduced ductility [56,58,59]. The combined effect of Al and C, as presented with CoFeMnNi in this work, opens up

new ways for the mechanism-based and lightweight-oriented design of MPEAs. Whereas the addition of C to Al-free MPEAs may be used to promote the TRIP-to-TWIP transition due to a SFE increase [70], it can also be used to tailor the slip-to-TWIP transition due to a SFE decrease in Al-containing MPEAs.

In summary, DFT-based SFE calculations were performed in the $\text{Al}_x\text{C}_y\text{CoFeMnNi}$ system to evaluate the effect of Al and C. In contrast to CoFeMnNi and other fcc alloys, an increased C content in Al-alloyed CoFeMnNi was predicted to decrease the SFE because of a lower solution energy in the hcp phase. To evaluate the reliability of the predictions, $\text{Al}_{0.26}\text{C}_y\text{CoFeMnNi}$ samples were produced by LPBF with up to 2.70 at% C. With increasing C content, higher strain hardening rates and twin volume fractions were observed experimentally, resulting in higher strength and ductility. Therefore, the experimental results confirm the predictive power and applicability of the used DFT-based concept. This highlights that combined DFT, computational thermodynamics and rapid sample production using LPBF is a promising and efficient approach for fast screening and design of MPEAs. Furthermore, specifically alloying fcc-based MPEAs with Al and C paves the way for mechanism-based design of these alloys and enables to overcome the strength-ductility trade-off.

Data availability

The raw/processed data required to reproduce these findings cannot be shared at this time as the data also forms part of an ongoing study.

Declaration of competing interest

The authors confirm that there are no known conflicts of interest associated with this publication and there has been no significant financial support beside the stated ones for this work that could have influenced its outcome.

Acknowledgments

F.Ki., Y.I., B.H., F.Kö. and C.H. would like to thank the *Deutsche Forschungsgemeinschaft* (DFG, German Research Foundation) for the support of the depicted research within the priority programme 2006 “CCA – HEA” (project-IDs 388166069 and 388544551). F.Ki., S.E., J.H.S. and C.H. also gratefully acknowledge the support by the Hans Hermann Voss-Stiftung within the RWTH Aachen Seed-Fund project OPSF406 (G:(DE-82)ZUK2-SF-OPSF406). S.E., J.H.S. and C.H. also gratefully acknowledge the funding of the DFG under Germany’s Excellence Strategy - EXC-2023 Internet of Production - 390621612.

Supplementary material

Supplementary material associated with this article can be found, in the online version, at doi:10.1016/j.scriptamat.2019.12.004.

References

- [1] D.B. Miracle, O.N. Senkov, *Acta Mater.* 122 (2017) 448–511, doi:10.1016/j.actamat.2016.08.081.
- [2] E.P. George, D. Raabe, R.O. Ritchie, *Nat. Rev. Mater.* 4 (8) (2019) 1, doi:10.1038/s41578-019-0121-4.
- [3] B. Murty, J. Yeh, S. Ranganathan, P. Bhattacharjee, in: B. Murty, J. Yeh, S. Ranganathan, P. Bhattacharjee (Eds.), *High-Entropy Alloys*, 2, Elsevier, 2019, pp. 1–12, doi:10.1016/B978-0-12-816067-1.00001-1.
- [4] B. Cantor, I.T. Chang, P. Knight, A.J. Vincent, *Mater. Sci. Eng. A* 375–377 (1–2 SPEC. ISS.) (2004) 213–218, doi:10.1016/j.msea.2003.10.257.
- [5] J.W. Yeh, S.K. Chen, S.J. Lin, J.Y. Gan, T.S. Chin, T.T. Shun, C.H. Tsau, S.Y. Chang, *Adv. Eng. Mater.* 6 (5) (2004) 299–303+274, doi:10.1002/adem.200300567.

- [6] S. Allain, J.P. Chateau, O. Bouaziz, Mater. Sci. Eng. A 387–389 (1–2 SPEC. ISS.) (2004) 143–147, doi:10.1016/j.msea.2004.01.060.
- [7] A. Saeed-Akbari, J. Imlau, U. Prah, W. Bleck, Metall. Mater. Trans. A 40 (13) (2009) 3076–3090, doi:10.1007/s11661-009-0050-8.
- [8] A. Saeed-Akbari, L. Mosecker, A. Schwedt, W. Bleck, Metall. Mater. Trans. A 43 (5) (2012) 1688–1704, doi:10.1007/s11661-011-0993-4.
- [9] B.C. De Cooman, Y. Estrin, S.K. Kim, Acta Mater. 142 (2018) 283–362, doi:10.1016/j.actamat.2017.06.046.
- [10] Z. Li, K.G. Pradeep, Y. Deng, D. Raabe, C.C. Tasan, Nature 534 (7606) (2016) 227–230, doi:10.1038/nature17981.
- [11] C. Haase, L.A. Barrales-Mora, Metals 9 (7) (2019) 726, doi:10.3390/met9070726.
- [12] D.B. Miracle, J.D. Miller, O.N. Senkov, C. Woodward, M.D. Uchic, J. Tiley, Entropy 16 (1) (2014) 494–525, doi:10.3390/e16010494.
- [13] K.G. Pradeep, C.C. Tasan, M.J. Yao, Y. Deng, H. Springer, D. Raabe, Mater. Sci. Eng. A 648 (2015) 183–192, doi:10.1016/j.msea.2015.09.010.
- [14] C. Haase, F. Tang, M.B. Wilms, A. Weisheit, B. Hallstedt, Mater. Sci. Eng. A 688 (January) (2017) 180–189, doi:10.1016/j.msea.2017.01.099.
- [15] F. Kies, P. Köhnen, M.B. Wilms, F. Brasche, K.G. Pradeep, A. Schwedt, S. Richter, A. Weisheit, J.H. Schleifenbaum, C. Haase, Mater. Des. 160 (2018) 1250–1264, doi:10.1016/j.matdes.2018.11.051.
- [16] S. Ewald, F. Kies, S. Hermsen, M. Voshage, C. Haase, J.H. Schleifenbaum, Materials 12 (10) (2019) 1706, doi:10.3390/ma12101706.
- [17] B. Hallstedt, A.V. Khvan, B.B. Lindahl, M. Selleby, S. Liu, Calphad 56 (2017) 49–57, doi:10.1016/j.calphad.2016.11.006.
- [18] Y. Ikeda, B. Grabowski, F. Körmann, Mater. Charact. 147 (2019) 464–511, doi:10.1016/j.matchar.2018.06.019.
- [19] A.J. Zaddach, C. Niu, C.C. Koch, D.L. Irving, JOM 65 (12) (2013) 1780–1789, doi:10.1007/s11837-013-0771-4.
- [20] S. Huang, W. Li, S. Lu, F. Tian, J. Shen, E. Holmström, L. Vitos, Scr. Mater. 108 (2015) 44–47, doi:10.1016/j.scriptamat.2015.05.041.
- [21] L. Patriarca, A. Ojha, H. Sehitoglu, Y.I. Chumlyakov, Scr. Mater. 112 (2016) 54–57, doi:10.1016/j.scriptamat.2015.09.009.
- [22] M. Beyramali Kiviy, M. Asle Zaeem, Scr. Mater. 139 (Supplement C) (2017) 83–86, doi:10.1016/j.scriptamat.2017.06.014.
- [23] Z. Li, F. Körmann, B. Grabowski, J. Neugebauer, D. Raabe, Acta Mater. 136 (2017) 262–270, doi:10.1016/j.actamat.2017.07.023.
- [24] Y.H. Zhang, Y. Zhuang, A. Hu, J.J. Kai, C.T. Liu, Scr. Mater. 130 (2017) 96–99, doi:10.1016/j.scriptamat.2016.11.014.
- [25] Z. Zhang, H. Sheng, Z. Wang, B. Gludovatz, Z. Zhang, E.P. George, Q. Yu, S.X. Mao, R.O. Ritchie, Nat. Commun. 8 (2017) 14390, doi:10.1038/ncomms14390.
- [26] S. Zhao, G.M. Stocks, Y. Zhang, Acta Mater. 134 (2017) 334–345, doi:10.1016/j.actamat.2017.05.001.
- [27] S. Alkan, A. Ojha, H. Sehitoglu, Acta Mater. 147 (2018) 149–164, doi:10.1016/j.actamat.2017.12.058.
- [28] J. Ding, Q. Yu, M. Astar, R.O. Ritchie, Proc. Natl. Acad. Sci. 115 (36) (2018) 8919–8924, doi:10.1073/pnas.1808660115.
- [29] Z. Dong, S. Schönecker, W. Li, D. Chen, L. Vitos, Sci. Rep. 8 (1) (2018) 12211, doi:10.1038/s41598-018-30732-y.
- [30] H. Huang, X. Li, Z. Dong, W. Li, S. Huang, D. Meng, X. Lai, T. Liu, S. Zhu, L. Vitos, Acta Mater. 149 (2018) 388–396, doi:10.1016/j.actamat.2018.02.037.
- [31] S. Huang, H. Huang, W. Li, D. Kim, S. Lu, X. Li, E. Holmström, S.K. Kwon, L. Vitos, Nat. Commun. 9 (1) (2018) 2381, doi:10.1038/s41467-018-04780-x.
- [32] Y. Ikeda, F. Körmann, I. Tanaka, J. Neugebauer, Entropy 20 (9) (2018) 655, doi:10.3390/e20090655.
- [33] C. Niu, C.R. LaRosa, J. Miao, M.J. Mills, M. Ghazisaeidi, Nat. Commun. 9 (1) (2018) 1363, doi:10.1038/s41467-018-03846-0.
- [34] Y. Ikeda, I. Tanaka, J. Neugebauer, F. Körmann, Phys. Rev. Mater. 3 (11) (2019) 113603, doi:10.1103/PhysRevMaterials.3.113603.
- [35] B. Yin, W.A. Curtin, NPJ Comput. Mater. 5 (1) (2019) 14, doi:10.1038/s41524-019-0151-x.
- [36] S. Zhao, Y. Osetsky, G.M. Stocks, Y. Zhang, NPJ Comput. Mater. 5 (1) (2019) 13, doi:10.1038/s41524-019-0150-y.
- [37] H. Kim, D.-W.W. Suh, N.J. Kim, Sci. Technol. Adv. Mater. 14 (1) (2013) 014205, doi:10.1088/1468-6996/14/1/014205.
- [38] J.H. Ryu, S.K. Kim, C.S. Lee, D.W. Suh, H.K. Bhadeshia, Proc. R. Soc. A: Math. Phys. Eng. Sci. 469 (2149) (2013) 20120458, doi:10.1098/rspa.2012.0458.
- [39] P.J. Denteneer, W. Van Haeringen, J. Phys. C: Solid State Phys. 20 (32) (1987) L883–L887, doi:10.1088/0022-3719/20/32/001.
- [40] A. Zunger, S.H. Wei, L.G. Ferreira, J.E. Bernard, Phys. Rev. Lett. 65 (3) (1990) 353–356, doi:10.1103/PhysRevLett.65.353.
- [41] P.E. Blöchl, Phys. Rev. B 50 (24) (1994) 17953–17979, doi:10.1103/PhysRevB.50.17953.
- [42] J.P. Perdew, K. Burke, M. Ernzerhof, Phys. Rev. Lett. 77 (18) (1996) 3865–3868, doi:10.1103/PhysRevLett.77.3865.
- [43] G. Kresse, J. Non-Cryst. Solids 192–193 (0) (1995) 222–229, doi:10.1016/0022-3093(95)00355-X.
- [44] G. Kresse, J. Furthmüller, Comput. Mater. Sci. 6 (1) (1996) 15–50, doi:10.1016/0927-0256(96)00008-0.
- [45] G. Kresse, D. Joubert, Phys. Rev. B 59 (3) (1999) 1758–1775, doi:10.1103/PhysRevB.59.1758.
- [46] D. Ma, B. Grabowski, F. Körmann, J. Neugebauer, D. Raabe, Acta Mater. 100 (2015) 90–97, doi:10.1016/j.actamat.2015.08.050.
- [47] F. Bachmann, R. Hielscher, H. Schaeben, Ultramicroscopy 111 (12) (2011) 1720–1733, doi:10.1016/j.ultramic.2011.08.002.
- [48] G. Nolze, R. Hielscher, J. Appl. Crystallogr. 49 (5) (2016) 1786–1802, doi:10.1107/S1600576716012942.
- [49] X. Zhang, B. Grabowski, F. Körmann, A.V. Ruban, Y. Gong, R.C. Reed, T. Hickel, J. Neugebauer, Phys. Rev. B 98 (22) (2018) 224106, doi:10.1103/PhysRevB.98.224106.
- [50] Z. Li, F. Körmann, B. Grabowski, J. Neugebauer, D. Raabe, Acta Mater. 136 (2017) 262–270, doi:10.1016/j.actamat.2017.07.023.
- [51] X. Zhang, B. Grabowski, T. Hickel, J. Neugebauer, Comput. Mater. Sci. 148 (2018) 249–259, doi:10.1016/j.commatsci.2018.02.042.
- [52] Z. Wu, C.M. Parish, H. Bei, J. Alloys Compd. 647 (2015) 815–822, doi:10.1016/j.jallcom.2015.05.224.
- [53] N.D. Stepanov, N.Y. Yurchenko, M.A. Tikhonovsky, G.A. Salishchev, J. Alloys Compd. 687 (2016) 59–71, doi:10.1016/j.jallcom.2016.06.103.
- [54] J. Chen, Z. Yao, X. Wang, Y. Lu, X. Wang, Y. Liu, X. Fan, Mater. Chem. Phys. 210 (2017) 136–145, doi:10.1016/j.matchemphys.2017.08.011.
- [55] J.Y. Ko, S.I. Hong, J. Alloys Compd. 743 (2018) 115–125, doi:10.1016/j.jallcom.2018.01.348.
- [56] Z. Li, Acta Mater. 164 (2018) 400–412, doi:10.1016/j.actamat.2018.10.050.
- [57] X.W. Liu, L. Liu, G. Liu, X.X. Wu, D.H. Lu, J.Q. Yao, W.M. Jiang, Z.T. Fan, W.B. Zhang, Metall. Mater. Trans. A 49 (6) (2018) 2151–2160, doi:10.1007/s11661-018-4549-8.
- [58] H. TianDang, J. Li, Z. ChangLiang, J. Hui, L. YiPing, L. TingJu, Sci. China 61 (1) (2018) 117–123, doi:10.1007/s11431-017-9134-6.
- [59] L. Guo, X. Ou, S. Ni, Y. Liu, M. Song, Mater. Sci. Eng. A 746 (December 2018) (2019) 356–362, doi:10.1016/j.msea.2019.01.050.
- [60] I. Gutierrez-Urrutia, D. Raabe, Acta Mater. 59 (16) (2011) 6449–6462, doi:10.1016/j.actamat.2011.07.009.
- [61] S. Kang, J.G. Jung, M. Kang, W. Woo, Y.K. Lee, Mater. Sci. Eng. A 652 (2016) 212–220, doi:10.1016/j.msea.2015.11.096.
- [62] C. Haase, L.A. Barrales-Mora, Acta Mater. 150 (2018) 88–103, doi:10.1016/j.actamat.2018.02.048.
- [63] G. Gottstein, Materialwissenschaft und Werkstofftechnik, 4, Springer-Verlag Berlin Heidelberg, 2014, doi:10.1002/ciuz.201390048.
- [64] G. Laplanche, P. Gadaud, O. Horst, F. Otto, G. Eggeler, E.P. George, J. Alloys Compd. 623 (2015) 348–353, doi:10.1016/j.jallcom.2014.11.061.
- [65] A. Haglund, M. Koehler, D. Catoor, E.P. George, V. Keppens, Intermetallics 58 (2015) 62–64, doi:10.1016/j.intermet.2014.11.005.
- [66] P. Köhnen, M. Létang, M. Voshage, J.H. Schleifenbaum, C. Haase, Addit. Manuf. 30 (2019) 100914, doi:10.1016/j.addma.2019.100914.
- [67] C. Haase, J. Bültmann, J. Hof, S. Ziegler, S. Bremen, C. Hinke, A. Schwedt, U. Prah, W. Bleck, Materials 10 (1) (2017) 56, doi:10.3390/ma10010056.
- [68] I. Gutierrez-Urrutia, S. Zaeferrer, D. Raabe, Mater. Sci. Eng. A 527 (15) (2010) 3552–3560, doi:10.1016/j.msea.2010.02.041.
- [69] S. Sevsek, F. Brasche, C. Haase, W. Bleck, Mater. Sci. Eng. A 746 (2019) 434–442, doi:10.1016/j.msea.2019.01.042.
- [70] Z. Li, C.C. Tasan, H. Springer, B. Gault, D. Raabe, Sci. Rep. 7 (2017) 40704, doi:10.1038/srep40704.